
Article:
Mir, ZS orcid.org/0000-0003-2223-2833, Lewis, TR, Onel, L et al. (3 more authors) (2020) CH_2OO Criegee intermediate UV absorption cross-sections and kinetics of CH_2OO + CH_2OO and CH_2OO + I as a function of pressure. Physical Chemistry Chemical Physics, 22 (17). pp. 9448-9459. ISSN 1463-9076

https://doi.org/10.1039/D0CP00988A

CH_2OO Criegee Intermediate UV absorption cross-sections and kinetics of CH_2OO + CH_2OO and CH_2OO + I as a function of pressure

Zara S. Mir,[1] Thomas R. Lewis,[1] Lavinia Onel,[1] Mark A. Blitz,[1,2] Paul W. Seakins,[1] Daniel Stone[1*]

[1]School of Chemistry, University of Leeds, [2]National Centre for Atmospheric Science, University of Leeds

*Corresponding author: d.stone@leeds.ac.uk

Abstract

The UV absorption cross-sections of the Criegee intermediate CH_2OO, and kinetics of the CH_2OO self-reaction and the reaction of CH_2OO with I are reported as a function of pressure at 298 K. Measurements were made using pulsed laser flash photolysis of $CH_2I_2/O_2/N_2$ gas mixtures coupled with time-resolved broadband UV absorption spectroscopy at pressures between 6 and 300 Torr. Results give a peak absorption cross-section of $(1.37 \pm 0.29) \times 10^{-17}$ cm^2 at ~340 nm and a rate coefficient for the CH_2OO self-reaction of $(8.0 \pm 1.1) \times 10^{-11}$ cm^3 s^{-1}, with no significant pressure dependence of the absorption cross-sections or the self-reaction kinetics over the range investigated. The rate coefficient for the reaction between CH_2OO and I demonstrates pressure dependence over the range investigated, with a Lindemann fit giving $k_0 = (4.4 \pm 1.0) \times 10^{-29}$ cm^6 s^{-1} and $k_\infty = (6.7 \pm 0.6) \times 10^{-11}$ cm^3 s^{-1}. The origins of IO in the system have been investigated, the implications of which are discussed.

Introduction

Oxidation chemistry is responsible for the removal of volatile organic compounds (VOCs) and other primary pollutants such as SO_2 and NO_x (NO_x = NO + NO_2) from the atmosphere, whilst also potentially leading to the production of secondary pollutants such as ozone and secondary organic aerosol (SOA). Globally, the O_3-initiated oxidation of unsaturated VOCs in ozonolysis reactions removes ~10 % of isoprene (C_5H_8),[1] the dominant VOC emitted into the atmosphere, and ozonolysis reactions make significant contributions to the tropospheric oxidising capacity at night and in winter when photochemistry is limited by the low intensity of solar radiation.[2-4] Ozonolysis reactions lead to the cleavage of C=C double bonds, resulting in production of a carbonyl product and a carbonyl oxide, which is referred to as a Criegee intermediate. The Criegee intermediate is zwitterionic in character, and is typically formed with high internal energy which leads to a competition between decomposition, producing species such as OH and HO_2,[5-9] and collisional stabilisation to produce a stabilised Criegee intermediate.[6, 10]

Since the discovery of photolytic methods to produce collisionally stabilised Criegee intermediates (SCIs) in the laboratory[11] there have been a large number of studies of SCI reaction kinetics, suggesting that SCI reactions with water dimers,[12-15] SO_2[11, 16-24] and organic acids,[25, 26] among others, may be significant in the atmosphere. Measurements of the UV absorption cross-sections of CH_2OO, the simplest Criegee intermediate, have indicated that the absorption cross-sections are relatively large, on the order of ~10^{-17} cm^2,[16, 27-29] thus making UV absorption spectroscopy a useful tool for the measurement of atmospherically relevant SCI reaction kinetics. However, there are significant discrepancies in the absolute cross-sections reported, and in the shape of the spectrum. Experiments have also shown a rapid CH_2OO + CH_2OO self-reaction,[19, 30-32] the kinetics of which can be closely coupled to the measurement of the absorption cross-sections, since significant changes in concentration can occur on the timescale of the absorption measurements. The reaction between CH_2OO and I is potentially important in laboratory experiments using CH_2I_2 photolysis to generate CH_2OO, and could also be of significance in the upper troposphere owing to the low H_2O content in such regions and the resulting longer lifetimes of CH_2OO.[33]

A combination of electronic structure and Frank Condon factor calculations were used to predict the features of the CH_2OO UV spectrum, indicating the presence of a broad, but intense, absorption band in the region 250-450 nm owing to the $\tilde{B}^1A' \leftarrow \tilde{X}^1A'$ transition.[34, 35] The calculations also suggested that the spectrum would exhibit extensive vibronic structure, owing to excitation of O-O stretching modes and C-O-O bending modes, and that there were hints of CH_2OO absorption in previous measurements of the UV spectrum of CH_2IO_2.[36]

The first measurements of the UV spectrum of CH_2OO were reported by Beames *et al.*,[27] in which an action spectrum was observed by monitoring the change in the CH_2OO photoionisation signal on irradiation with UV light generated by a tunable Nd:YAG pumped dye laser at wavelengths between 280 and 420 nm. A pulsed valve system was used to produce jet cooled CH_2OO following photolysis of CH_2I_2 at λ = 248 nm in the presence of O_2 in Ar at ~1300 Torr, with CH_2OO monitored following single photon photoionisation at λ = 118 nm. Excitation of CH_2OO from the ground electronic state on irradiation with UV light resulted in depletion of the photoionisation signal, with the extent of depletion combined with knowledge of the UV photon flux to determine the cross-sections. The spectrum was observed to be broad in the wavelength region 300 – 370 nm, with a maximum cross-section of $(5.0 \pm 0.7) \times 10^{-17}$ cm^2 at λ ~ 335 nm, indicating an atmospheric lifetime of CH_2OO of ~ 1 s at midday with respect to solar photolysis. In a subsequent paper by the same group investigating the UV absorption spectrum of the alkyl-substituted Criegee intermediate CH_3CHOO using the same experimental technique, it was determined that experimental factors, such as homogeneity of the laser beam and laser-molecular beam overlap, suggested an uncertainty in absolute cross-section measurements on the order of a factor of 2.[37]

A broad UV spectrum was also reported by Sheps[16] using time-resolved broadband cavity-enhanced absorption spectroscopy at a temperature of 295 K and a pressure of 5.1 Torr, with the improved wavelength resolution of the technique revealing the significant vibronic structure at longer wavelengths predicted previously.[34] However, the direct absorption measurements demonstrated a wider absorption spectrum than observed for the action spectrum,[27] with a lower peak absorption cross-section of $(3.6 \pm 0.9) \times 10^{-17}$ cm^2 occurring at a longer wavelength of ~355 nm. The cavity-enhanced measurements used photolysis of $CH_2I_2/O_2/He$ mixtures at λ = 266 nm, leading to the total observed absorbance containing overlapping contributions from CH_2OO, the depletion of CH_2I_2, and the production of IO radicals from unavoidable secondary chemistry occurring in the reaction system. Separation of the spectral contributions was achieved by the addition of SO_2 to the reaction system to aid identification of the contribution from CH_2OO. Scaling of the total absorbance observed following complete removal of CH_2OO by SO_2 to the time dependence of the absorbance signal in a region of the spectrum dominated by IO absorption, and subtraction of the scaled spectrum from the total absorbance observed at each time point in the experiment enabled identification of the CH_2OO absorbance, assuming that the time dependence of CH_2I_2 is negligible. Kinetic fitting of the time dependence of the CH_2OO signal enabled determination of the CH_2OO absorbance immediately following photolysis (i.e. at t = 0). Separate experiments to measure the CH_2I absorbance combined with knowledge of the CH_2OO yields from $CH_2I + O_2$[38-40] gave the absolute CH_2OO concentration produced in the system (~5×10^{11} cm^{-3}). Absolute absorption cross-sections for CH_2OO could then be ascertained from the Beer-Lambert law using the total absorption path length, which was measured to be 40-56 m across the spectral range by measuring the well-characterised absorbance spectra of known concentrations of NO_2 and CH_2I_2.

The UV absorption cross-sections of CH_2OO were also reported by Ting *et al.*,[28] using photolysis of $CH_2I_2/O_2/N_2$ at λ = 248 nm to generate CH_2OO. Transient absorption spectroscopy was used to obtain the total absorbance in the reaction system, which, similarly to the work of Sheps,[16] contained significant contributions from CH_2I_2 and IO. Separation of the contribution from IO to the total absorbance was achieved by using the characteristic vibronic structure in the IO spectrum to identify and subtract the contribution from IO at each time point. The CH_2I_2 contribution was determined by subtracting the IO-corrected absorbance at a time point following complete reaction of CH_2OO, when only CH_2I_2 contributes to the IO-corrected absorbance, from an early time point, when both CH_2I_2 and CH_2OO contribute. Experiments were performed in which CH_2OO

removal was dominated by CH_2OO self-reaction, and in which SO_2 was added to increase the removal rate via $CH_2OO + SO_2$. Initial concentrations of CH_2OO were determined to be ~10^{13} cm^{-3} by measurements of CH_2I absorbance and the known yield of CH_2OO from $CH_2I + O_2$, and were used to obtain a peak CH_2OO absorption cross-section of $(1.26 \pm 0.25) \times 10^{-17}$ cm^2 at λ ~ 340 nm. The spectral shape observed by Ting *et al*. was similar to that reported by Sheps, with significant vibronic structure at λ > 340 nm.[16] Cross-sections at λ = 308.4 nm and at λ = 351.8 nm were also measured independently by Ting *et al*. in a molecular beam experiment to monitor the effects of UV laser irradiation on CH_2OO ion signals, obtained by electron impact ionisation and quadrupole mass spectrometry,[28] with similarities to the experiments performed by Beames *et al*.[27] The molecular beam experiments gave cross-sections of $\sigma = (8.09 \pm 0.90) \times 10^{-18}$ cm^2 at λ = 308.4 nm and $\sigma \leq (1.21 \pm 0.13) \times 10^{-17}$ cm^2 at λ = 351.8 nm, which scale to a peak cross-section of $(1.23 \pm 0.18) \times 10^{-17}$ cm^2 at λ ~ 340 nm.

Subsequent experiments by Foreman *et al*.[29] using photolysis of $CH_2I_2/O_2/N_2$ at λ = 355 nm with single-pass broadband absorption spectroscopy at a total pressure of 50 Torr over the temperature range 276-357 K, and cavity ringdown spectroscopy at a total pressure of 70 Torr and room temperature, were carried out to determine high resolution absorption cross-sections at wavelengths between 362 and 470 nm. Contributions to the total absorbance from CH_2I_2 were negligible over the wavelength range under consideration, while those from IO were subtracted in a similar method to that employed by Ting *et al*.[28] Measurements of the initial CH_2I_2 concentration and photolysis laser fluence were used to estimate the initial CH_2I concentration, and thus the initial CH_2OO concentration (~1.5×10^{13} cm^{-3} for broadband absorption measurements and ~5×10^{12} cm^{-3} for cavity ringdown measurements, with an estimated uncertainty of ~28% for both types of measurement) from the measured yields of $CH_2I + O_2$. The results of both the absorption measurements and the cavity ringdown experiments showed good agreement with both the spectral shape and absolute cross-sections reported by Ting *et al*.,[28] and indicated no significant temperature dependence of the cross-sections and no rotational fine structure in any of the vibronic features in the spectrum.

Self-reaction kinetics of CH_2OO were first reported by Su *et al*.[30] using flash photolysis of $CH_2I_2/O_2/N_2$ at λ = 355 nm with transient infrared spectroscopy to monitor CH_2OO throughout the reaction. Observed decays of CH_2OO were analysed considering potential loss of CH_2OO through reaction with I atoms and CH_2I radicals as well as loss through the CH_2OO self-reaction, with results indicating a rate coefficient of $(4 \pm 2) \times 10^{-10}$ cm^3 s^{-1} at 343 K at total pressures between 20 and 100 Torr. Such a rapid reaction was attributed to the zwitterionic nature of CH_2OO, but theory predicts a significantly lower rate coefficient of ~4×10^{-11} cm^3 s^{-1}.[41]

Buras *et al*.[31] observed a rate coefficient of $(6.0 \pm 2.1) \times 10^{-11}$ cm^3 s^{-1} at 297 K using flash photolysis of CH_2I_2/O_2 at λ = 266 nm in N_2 and He at total pressures between 25 and 100 Torr. CH_2OO was monitored by UV absorption spectroscopy at λ = 375 nm with simultaneous near-infrared absorption measurements of I atoms to quantify the initial CH_2OO concentration and investigate the role of CH_2OO + I. These measurements also enabled determination of the CH_2OO absorption cross-section at 375 nm, which was found to be in agreement with the results of Ting *et al*.,[28] and indicated an upper limit of 1.0×10^{-11} cm^3 s^{-1} for the rate coefficient for CH_2OO + I, and as a result the reaction was reported to have no significant impact on the observed CH_2OO decays.

Further experiments by Ting *et al*.,[32] using flash photolysis of $CH_2I_2/O_2/N_2$ at λ = 248 nm with broadband transient UV spectroscopy, were performed to investigate the kinetics of the CH_2OO self-reaction at 295 K at pressures between 7.6 and 779 Torr. Temporal profiles of CH_2OO and IO, obtained by deconvoluting the total observed absorbances through knowledge of the CH_2OO and IO absorption cross-sections, were fitted to a detailed chemical mechanism using numerical integration to determine a rate coefficient for the CH_2OO self-reaction of $(8 \pm 4) \times 10^{-11}$ cm^3 s^{-1}. However, the results were observed to be sensitive to the kinetics of the reaction between CH_2OO and I, in contrast to the observations of Buras *et al*.,[31] with the best fit to the data giving a rate coefficient of ~8×10^{-11} cm^3 s^{-1} for CH_2OO + I.[32]

Cavity ringdown spectroscopy has also been used by Chhantyal-Pun *et al.*[19] to monitor CH_2OO at λ = 355 nm to determine the self-reaction kinetics of CH_2OO, using flash photolysis of $CH_2I_2/O_2/N_2$ at λ = 355 nm at 293 K over the pressure range 7-30 Torr. Initially, the observed decays were fit to an analytical solution describing a mixed first- and second-order loss of CH_2OO to find the first-order component to the loss. However, the second-order component to the loss was found to depend on the total pressure in the system, indicating the presence of second-order losses other than CH_2OO self-reaction. Fits to the data obtained at 7 Torr using numerical integration and considering losses through CH_2OO self-reaction and CH_2OO + I showed no significant contribution from CH_2OO + I, in agreement with the results of Buras *et al.*,[31] and gave a rate coefficient of $(7.35 \pm 0.63) \times 10^{-11}$ cm^3 s^{-1} for the CH_2OO self-reaction. Although the results at 7 Torr were not significantly affected by CH_2OO + I, it is likely that the results obtained at higher pressures were impacted by CH_2OO + I which is evident from the increase in the rate of CH_2OO loss as the pressure is increased.

Discrepancies in the reported absorption cross-sections for CH_2OO, and in the kinetics for the CH_2OO self-reaction and reaction between CH_2OO and I, have consequences for our understanding of CH_2OO chemistry under both laboratory and atmospheric conditions. In this work we report UV absorption cross-sections of CH_2OO and kinetics of the CH_2OO self-reaction and the reaction of CH_2OO with I at 298 K as a function of pressure in the range 6 to 300 Torr using time-resolved broadband UV spectroscopy.

Experimental

The UV absorption cross-sections and self-reaction kinetics of the CH_2OO Criegee intermediate were studied using laser flash photolysis of $CH_2I_2/O_2/N_2$ gas mixtures, coupled with broadband time-resolved UV absorption spectroscopy. The experimental apparatus has been described in detail elsewhere,[13, 42] therefore only a brief description is given here.

Precursor gases were mixed in a gas manifold at known flow rates determined by calibrated mass flow controllers (MKS Instruments), with CH_2I_2 introduced into the gas flow by passing a known slow flow of N_2 through a bubbler containing liquid CH_2I_2 at room temperature, and passed into a 1.5 m long glass reaction cell. The reaction cell was 54 mm inner diameter, and sealed with fused silica windows at both ends. The total flow rate was maintained at 4000 standard cm^3 per minute (sccm) at 100 Torr and adjusted accordingly with pressure to maintain constant number densities for reactant gases and a constant residence time in the cell of ~6 s. Total pressure in the cell was measured by a capacitance manometer (MKS Instruments) and controlled by a rotary pump (EM2, Edwards) by throttling the exit to the reaction cell. All experiments were performed at T = (298 ± 2) K in N_2 (BOC oxygen free, 99.998%) at pressures between 6 and 300 Torr. CH_2I_2 (Alfa Aesar 99%) concentrations were in the range $1 \times 10^{12} - 4 \times 10^{13}$ cm^{-3} and O_2 (BOC, 99.5 %) concentrations were varied between 1×10^{16} and 4×10^{17} cm^{-3}. Gases and chemicals were used as supplied.

Reactions R1-R5 were initiated in the reaction cell by an excimer laser (KrF, Lambda-Physik CompEx 210), operating at a wavelength of λ = 248 nm, which was aligned along the length of the reaction cell using a dichroic turning mirror (Edmund Optics). The timing of the photolysis laser was controlled by a delay generator (SRS DG535) with a pulse repetition rate of 0.15 Hz such that a fresh gas mixture was photolysed on each pulse. The typical laser fluence was ~25 mJ cm^{-2}, giving $[CH_2OO]_0$ on the order of ~10^{11} cm^{-3}.

$CH_2I_2 + h\nu$ (λ=248 nm)	→	$CH_2I + I$	(R1)
$CH_2I + O_2$	→	$CH_2OO + I$	(R2a)
$CH_2I + O_2$	→	CH_2IO_2	(R2b)
$CH_2OO + CH_2OO$	→	products	(R3)
$CH_2OO + I$	→	products	(R4)

CH_2OO → products (R5)

Absorption of UV/visible radiation by species within the cell was monitored using a laser-driven light source (LDLS, Energetiq EQ-99X), which provides ~10 mW cm^{-2} of light at wavelengths between 200 nm and 800 nm with near constant radiance across the spectral range. Output from the lamp was directed onto an off-axis parabolic mirror (ThorLabs) to collimate the beam. Approximately 10 % of the light was aligned along the length of the cell to give a single pass through the cell overlapping completely with the photolysis beam, with the remaining light aligned in the multi-pass arrangement described in detail in previous work.[42] In this work, the optics controlling the path of the multi-pass beam were arranged to give either 7 or 13 passes through the cell. The effective path length of the multi-pass arrangement was determined from the ratio of the absorbance of IO, which is produced by secondary chemistry in the system, observed using the multi-pass arrangement to that observed simultaneously in the single pass, which has a fixed and definite path length of 150 cm. Total effective path lengths of (443 ± 21) cm and (1136 ± 143) cm were obtained from the 7 and 13 pass arrangements, respectively, when considering the total overlap between the photolysis and probe beams.

The output beams from both the single and multi-pass arrangements were each passed through sharp cut-on filters (248 nm RazorEdge ultrasteep long-pass edge filter, Semrock) to minimise the impacts of scattered excimer light and focused onto fibre optics via fibre launchers (Elliot Scientific). Outputs from the fibre optics were directed onto spectrographs (CP140-103 Imaging Spectrograph, Horiba) and imaged onto line-scan charge-coupled device (CCD) detectors (S7030-1006 FFT, Hamamatsu), giving spectral resolution of 1.5 nm FWHM and time resolution of 1 ms. Wavelength calibration was performed via measurements of the well-known Hg emission spectrum from a low pressure Hg pen-ray lamp (Oriel). Timing of the cameras was controlled by the same delay generator used to control the firing of the excimer laser. Intensity data recorded by the cameras were typically averaged for 100 to 400 photolysis shots and were transferred to a PC for analysis.

Results

CH_2OO absorption cross-sections

Figure 1 shows the typical absorbance observed immediately following photolysis, with contributions from the absorbance of CH_2I_2 ($A_{CH2I2,t,\lambda}$), CH_2OO ($A_{CH2OO,t,\lambda}$) and IO ($A_{IO,t,\lambda}$):

$$A_{t,\lambda} = \ln(I_{0,\lambda}/I_{t,\lambda}) = A_{CH2I2,t,\lambda} + A_{CH2OO,t,\lambda} + A_{IO,t,\lambda} \quad \text{(Equation 1)}$$

where I_0 is the average light intensity at wavelength λ prior to photolysis and $I_{\lambda,t}$ is the light intensity at wavelength λ and time t following photolysis. The contribution from IO is readily distinguished by the strong vibronic structure in the region 400 to 450 nm and a fit of the IO reference spectrum[43] over this wavelength range was performed to remove the contribution from IO, giving $A'_{t,\lambda}$:

$$A'_{t,\lambda} = A_{t,\lambda} - A_{IO,t,\lambda} = A_{CH2I2,t,\lambda} + A_{CH2OO,t,\lambda} = \sigma_{CH2I2,\lambda}\,\Delta[CH_2I_2]\,l + \sigma_{CH2OO,\lambda}\,[CH_2OO]_t\,l \quad \text{(Equation 2)}$$

where $\sigma_{CH2I2,\lambda}$ is the CH_2I_2 absorption cross-section at wavelength λ, $\Delta[CH_2I_2]$ is the change in CH_2I_2 concentration on photolysis, $\sigma_{CH2OO,\lambda}$ is the CH_2OO absorption cross-section at wavelength λ, $[CH_2OO]_t$ is the concentration of CH_2OO at time t, and l is the path length of the light.

As described in previous work,[16, 28] since the CH_2I_2 concentration remains constant after photolysis, the absorbance owing to CH_2OO can be determined by subtraction of the absorbance $A'_{t,\lambda}$ at a late time point following photolysis (typically 50 ms after photolysis, when CH_2OO has reacted and $A'_{t,\lambda} = \sigma_{CH2I2,\lambda}\,\Delta[CH_2I_2]\,l$) from the absorbance $A'_{t,\lambda}$ at an earlier time point following photolysis (where $A'_{t,\lambda} = \sigma_{CH2I2,\lambda}\,\Delta[CH_2I_2]\,l + \sigma_{CH2OO,\lambda}\,[CH_2OO]_t\,l$). The average CH_2OO absorbance in the first 50 ms following photolysis was thus

determined and normalised to the maximum absorbance to determine the overall shape and position of the CH_2OO spectrum.

Absorption cross-sections for CH_2I_2[43] and the normalised CH_2OO spectrum were subsequently fit to $A'_{t,\lambda}$ at each time point to find $\Delta[CH_2I_2]\ l$ and the product of the maximum CH_2OO cross-section ($\sigma_{CH2OO,max}$) and $[CH_2OO]_t\ l$. A typical fit is shown in Figure 1. The yield of CH_2OO following photolysis of CH_2I_2 in the presence of O_2 has been measured previously in this laboratory,[40] and was used to determine $[CH_2OO]_{t=0}\ l$ from $\Delta[CH_2I_2]\ l$.

The time-profile of the product $\sigma_{CH2OO,max}\ [CH_2OO]_t\ l$, determined from the fit of the CH_2I_2 cross-sections and normalised CH_2OO cross-sections was fit to a mixed first- and second-order analytical kinetic loss to determine $\sigma_{CH2OO,max}\ [CH_2OO]_{t=0}\ l$ and hence $\sigma_{CH2OO,max}$ (see Supplementary Information for further information). An advantage of this data analysis is that determination of $\sigma_{CH2OO,max}$ is independent of the path length, l, hence the value of l does not need to be known. While the kinetic fits performed to determine $\sigma_{CH2OO,max}$ do provide some information regarding the kinetics of CH_2OO loss in the system, a more detailed analysis, described below, was performed to determine the CH_2OO self-reaction kinetics to enable investigation of secondary chemistry within the system.

The absorption cross-sections for CH_2OO determined in this work are shown in Figure 2 and are provided in the Supplementary Information. Results from this work indicate a maximum absorption cross-section of $(1.37 \pm 0.29) \times 10^{-17}$ cm^2 at a wavelength of ~340 nm, with no significant dependence on pressure in the range 6 to 300 Torr (see Supplementary Information for further details) in agreement with previous work by Ting *et al.*[28] which reports a maximum cross-section of $(1.23 \pm 0.18) \times 10^{-17}$ cm^2 at a wavelength of ~340 nm. Discrepancies in the position and absolute value of the maximum cross-section between the spectrum reported by Ting *et al.*[28] and those reported by Beames *et al.*[27] and Sheps[16] have been discussed in detail in previous work.[28, 29, 44] Figure 2 shows a comparison of the CH_2OO UV absorption cross-sections determined in this work with those reported in previous work. Vibronic structure is evident at wavelengths above 360 nm in the CH_2OO spectrum observed in this work, with eight bands observable, in agreement with previous work by Sheps,[16] Ting *et al.*[28] and Foreman *et al.*[29] Table 1 shows the band centres for the vibronic features observed in the CH_2OO spectrum, indicating good agreement between the results obtained in this work and those reported by Ting *et al.*[28] and Foreman *et al.*[29]

CH_2OO reaction kinetics

Concentrations for CH_2OO were determined from the fits to $A'_{t,\lambda}$ described above (Equation 2), which gave the product $\sigma_{CH2OO,max}\ [CH_2OO]_t\ l$, using $\sigma_{CH2OO,max} = (1.37 \pm 0.29) \times 10^{-17}$ cm^2 and knowledge of the path length ($l = (443 \pm 21)$ cm for 7 passes of the probe beam or $l = (1136 \pm 143)$ cm for 13 passes of the probe beam).

Kinetics describing the observed CH_2OO decays were fit with the numerical integration package FACSIMILE[45] using the mechanism shown in Table 2. Fits were performed globally at each pressure investigated to determine the rate coefficients for the CH_2OO self-reaction (k_3), $CH_2OO + I$ (k_4) and the first-order rate coefficient (k_5) describing CH_2OO loss by diffusion out of the probe beam, with the initial CH_2OO concentration as a local parameter for each trace in the global fit. Initial concentrations of CH_2I, I and CH_2IO_2 were determined from their relationship to the initial CH_2OO concentrations using our previous measurements of the yields of $CH_2I + O_2$ (R2) as a function of pressure.[40] At each pressure, a range of initial CH_2OO concentrations was used in order to provide greater sensitivity to the second-order components of the loss (k_3 and k_4) over the first-order components of the loss (k_5). Typical fits are shown in Figure 3.

The rate coefficient for the CH_2OO self-reaction was not observed to display any significant dependence on pressure, as shown in Figure 4 and Table 3, with an average value of $k_3 = (8.0 \pm 1.1) \times 10^{-11}$ cm^3 s^{-1} over all pressures. The uncertainty is the 1σ standard deviation of the mean value for all pressures combined with the

uncertainties determined from the sensitivity analysis described in detail below. A summary of results reported in previous work is given in Table 4, and a comparison of results obtained in this work with values previously reported in the literature is shown in Figure 4. Results from this work are in agreement with those reported by Ting *et al.*,[32] Buras *et al.*[31] and the results of Chhantyal-Pun *et al.* at 7 Torr,[19] which are all significantly lower than that reported by Su *et al.*[30] at a temperature of 343 K using infrared absorption spectroscopy.

Figure 5 shows the rate coefficient obtained in this work for the reaction between CH_2OO and I as a function of pressure, with values at each pressure given in Table 3. This work shows significant pressure dependence in the kinetics for CH_2OO + I, with k_4 varying from $(1.1\ ^{+2.2}_{-1.1}) \times 10^{-12}$ cm^3 s^{-1} at 6 Torr to $(5.5 \pm 2.1) \times 10^{-11}$ cm^3 s^{-1} at 300 Torr. A Lindemann fit (Equation 3) to the observed kinetics as a function of pressure gives $k_{4,0}$ = $(4.4 \pm 1.0) \times 10^{-29}$ cm^6 s^{-1} and $k_{4,\infty} = (6.7 \pm 0.6) \times 10^{-11}$ cm^3 s^{-1}, where the uncertainty is the 1σ standard deviation of the fit.

$$k_4 = k_{4,0}\,[\mathrm{M}]\,k_{4,\infty} \big/ (k_{4,0}\,[\mathrm{M}] + k_{4,\infty}) \qquad \text{(Equation 3)}$$

Previous studies of the CH_2OO self-reaction have indicated varying impacts of the reaction between CH_2OO and I. Table 4 summarises the range of values for k_4 that have been reported in the literature. Buras *et al.*[31] reported an upper limit for k_4 of 1×10^{-11} cm^3 s^{-1} on the basis of measurements of both CH_2OO and I atoms. These measurements, performed between 25 and 100 Torr at 297 K with initial concentrations on the order of 10^{12}-10^{13} cm^{-3}, indicated that the kinetics of I atom loss were independent of the initial concentrations of CH_2OO or I, and were dominated by diffusion. Chhantyal-Pun *et al.*[19] also reported an upper limit of 1×10^{-11} cm^3 s^{-1} for k_4 for experiments at 7 Torr and 293 K, although clear secondary chemistry was observed to impact the loss of CH_2OO at pressures above 7 Torr. The pressure dependence observed in the kinetics describing the loss of CH_2OO in the experiments by Chhantyal-Pun *et al.* was attributed to changes in the CH_2IO_2 yield from $CH_2I + O_2$ as a function of pressure and a potential reaction between CH_2OO and CH_2IO_2. The results of Su *et al.*[30] indicated $k_4 = (4 \pm 2) \times 10^{-11}$ cm^3 s^{-1} between 10 and 100 Torr, in broad agreement with the results of this work but it should be noted that experiments were conducted at 343 K and gave a significantly higher value for k_3 than determined in this work and in other studies. Experiments performed by Ting *et al.*[32] over a range of pressures (7.6 to 779 Torr) at 295 K also indicated significant impacts of CH_2OO + I on the loss of CH_2OO across the entire pressure range investigated, with the best fits to the observed CH_2OO decays giving pressure independent k_4 values in the range 6-10 $\times 10^{-11}$ cm^3 s^{-1}, in agreement with the high pressure limit obtained in this work. Thus, while there are significant discrepancies for k_4 reported in the literature, the pressure dependence observed in this work provides some insight as to the source of the discrepancies and reconciles the results of Chhantyal-Pun *et al.*[19] and Ting *et al.*,[32] with the results of Buras *et al.*[31] at low pressures within the experimental uncertainties of this work.

In order to investigate the sensitivity of k_3 and k_4 to the parameters used in the model (Table 2) to fit to the observed CH_2OO decays, each of the rate coefficients used in the model were sequentially doubled and halved and the effects on the fitted values of k_3 and k_4 were determined. Results from the sensitivity analysis are shown in Figure 6, and indicate no significant dependence of k_3 on the parameters used in the model. For k_4, the results indicate there is some sensitivity at low pressures to the rate coefficients used for R6-R9. The rate coefficients for R6-R8 used in the model shown in Table 2 are based on laser induced fluorescence measurements of IO and HCHO production following photolysis of $CH_2I_2/O_2/N_2$ at 100 Torr by Gravestock *et al.*,[36] and were obtained by fitting a model containing reactions R2b and R6-R8 to the experimentally observed HCHO, assuming that all CH_2IO produced in R6 spontaneously decomposes to HCHO + I. For R9, the rate coefficient used in the analysis is that used by Ting *et al.*, which is higher than the current IUPAC recommendation[46] but was required to adequately model the IO loss in the system, suggesting the presence of other loss processes for IO which could not be separated from IO + IO with any sensitivity. While there is some sensitivity of k_4 to R6-R9, uncertainties for k_4 reported in this work include uncertainties arising from sensitivity to the rate coefficients for R6-R9. The potential for reaction between CH_2OO and peroxy radicals (RO_2), such as CH_2IO_2, has been investigated in theoretical studies, with predicted rate coefficients for CH_2OO

316 + RO_2 reactions between 3.74×10^{-12} cm^3 s^{-1} and 1×10^{-11} cm^3 s^{-1}.[47-49] The impact of any such reaction on the
317 results reported in this work was investigated by incorporating a reaction between CH_2OO and CH_2IO_2 in the
318 model at the upper limit of the predicted rate coefficients for $CH_2OO + RO_2$. Results at 70 Torr were affected
319 by ~2 %, with those at 300 Torr affected by ~5 %. While the potential reaction between CH_2OO and CH_2IO_2
320 may not significantly impact the results reported here, reactions between Criegee intermediates and peroxy
321 radicals have been indicated to play important roles in the formation of highly oxidised species in the
322 atmosphere and warrant further studies.

323 Simulations were also performed to determine the sensitivity of the results for k_3 and k_4 on the products of
324 $CH_2OO + I$ specified in the model. Since the products, and branching ratios, of $CH_2OO + I$ are uncertain, fits
325 were performed in which the reaction was considered simply as a loss mechanism for CH_2OO and I (i.e. with
326 no products specified, as shown in Table 2), and in which varying branching ratios were considered for
327 production of $CH_2I + O_2$, CH_2IO_2, and $HCHO + IO$:

328 $$CH_2OO + I \rightarrow CH_2I + O_2 \quad \text{(R4a)}$$

329 $$CH_2OO + I \rightarrow CH_2IO_2 \quad \text{(R4b)}$$

330 $$CH_2OO + I \rightarrow HCHO + IO \quad \text{(R4c)}$$

331 The impacts on k_3 and k_4 of varying the branching ratios for channels R4a-c are shown in Figure 7. For k_3,
332 there is little sensitivity of the results to the nature of the products or branching ratio for R4. For k_4, there is
333 some sensitivity to the branching ratio adopted in the model, particularly at low pressures and if the reaction
334 proceeds primarily via R4a to form $CH_2I + O_2$. Although Su *et al*. predicted that production of $CH_2I + O_2$ is
335 the dominant reaction channel for R4, the kinetics of this reaction pathway are not expected to exhibit any
336 significant pressure dependence, and the lowest energy pathways in the reaction result in production of CH_2IO_2
337 or HCHO + IO. [30] R4a is expected to be thermodynamically unfeasible due to the existence of an activation
338 barrier to such a reaction, and since the forward reaction between CH_2I and O_2 has been shown to occur (R2a
339 and R2b) and is fast, the reverse reaction between CH_2OO and I to produce CH_2I and O_2 (R4a) is unlikely to
340 occur. Our previous measurements of the HCHO products of CH_2OO chemistry indicate that the CH_2OO self-
341 reaction and $CH_2OO + I$ ultimately produce HCHO in 100 % yield, either directly or via formation and
342 subsequent chemistry of CH_2IO_2.[18, 40] Ting *et al*.[32] have also indicated that channels producing CH_2IO_2 and
343 HCHO + IO are more significant than that producing $CH_2I + O_2$. We therefore exclude the possibility that the
344 reaction proceeds 100 % via R4a from further analysis. For all other combinations of branching ratios, the
345 results for k_4 are within 20 % of the value given by the model in which the reaction is treated as a loss
346 mechanism for CH_2OO and I but with products unspecified. Results reported for k_3 and k_4 in this work used
347 the model as shown in Table 2 (i.e. with products for R4 not specified) and include uncertainties resulting
348 from assumptions regarding the rate coefficients and branching ratios adopted in the model.

349 The production of IO following photolysis of CH_2I_2/O_2 mixtures has been investigated in a number of previous
350 studies, with several arguments proposed to explain the source of IO within the system. Early studies of the
351 reaction between CH_2I and O_2 indicated that IO was produced directly from $CH_2I + O_2$.[50-53] However, later
352 studies have provided evidence that IO is not produced directly from the reaction between CH_2I and O_2, but
353 is a product of secondary reactions involving I atoms.[32, 36, 54, 55] Dillon *et al*.[54] monitored the production of IO
354 using laser-induced fluorescence (LIF) spectroscopy following photolysis of CH_2I_2/O_2 at a wavelength of 351
355 nm at pressures between 15 and 60 Torr, and observed a non-linear dependence of the IO yield on the fluence
356 of the photolysis laser and on the concentration of O_2, suggesting an indirect radical-radical mechanism.
357 Subsequent work was carried out by Gravestock *et al*.,[36] in which IO was monitored via time-resolved
358 broadband UV absorption spectroscopy following photolysis of CH_2I_2/O_2 at wavelengths of 193 nm or 248
359 nm at room temperature and atmospheric pressure, under which conditions the chemistry of CH_2IO_2 dominates
360 over that of CH_2OO owing to the pressure dependent branching ratios for $CH_2I + O_2$. Gravestock *et al.*
361 observed a dependence of the production rate and yield of IO on the concentrations of CH_2I_2 and O_2, indicating

an indirect mechanism and leading to the suggestion that the production was dominated by the reaction between CH_2IO_2 and I. Ting *et al.*[32] have also indicated that production of IO at high pressures is dominated by CH_2IO_2 + I (R7), while production at lower pressures (p < 60 Torr) is dominated by CH_2OO + I (R4). Foreman and Murray[55] monitored the production of IO(v=0) and IO(v=1) using cavity ringdown spectroscopy following 355 nm photolysis of CH_2I_2/O_2 at 52 Torr and 295 K, with measurements indicating that the production of IO(v=0) was dominated by secondary chemistry, likely CH_2OO + I. Production of IO(v=1) was observed to occur with a rate coefficient five times larger than that for IO(v=0), but with a smaller yield, with results indicating direct production of IO(v=1) from the reaction of excited CH_2I^* with O_2 and a dependence of the mechanism on the degree of excitation of CH_2I.[55]

Figure 8 shows a typical IO concentration-time profile observed in this work. The profile is characterised by a rapid production of IO that occurs within 1 ms of photolysis, followed by a slower production and subsequent decay, as has been observed in previous studies.[36, 55] The peak IO concentration in this work was observed to be directly proportional to the initial concentration of CH_2I in the system (determined from the observed depletion in CH_2I_2 absorbance) with an IO yield that is ~20 % of the initial CH_2I concentration (see Supplementary Information for further details). Gravestock *et al.*[36] observed similar behaviour, but with a higher yield of 30-40 %, with results indicating that IO is not a direct photolysis product of CH_2I_2/O_2 but is produced via secondary radical processes. It was postulated that IO could be produced by a multi-photon process on photolysis of CH_2I_2 at 248 nm, leading to the production of CH_2 radicals which react rapidly with the excess O_2 to form HCHO + O, with subsequent production of IO through the reaction of O + CH_2I_2 → IO + CH_2I. However, this mechanism could only account for ~5 % of the IO observed in the system.[36] Subsequent work by Foreman and Murray[55] monitored production of both IO(v=0) and IO(v=1) by cavity ringdown spectroscopy following CH_2I_2/O_2 photolysis at 355 nm, with the observed behaviour suggesting production of excited CH_2I^* radials which generate IO on reaction with O_2. The impact of excited CH_2I^* on secondary production of HCHO and OH radicals has also been observed in other studies of CH_2OO chemistry.[18, 56]

In this work, we focus on the IO production in the system that occurs following the initial rapid production. Figure 9 shows the ratio of the maximum observed IO concentration to the concentration of IO generated by the initial rapid production, representing the yield of IO produced in the system following the initial rapid growth, as a function of pressure. The yield of IO was observed to increase with increasing pressure, with limited production of IO at low pressures. Model simulations constrained to the observed initial IO concentrations (i.e. the rapid IO production) were compared to the observed temporal behaviour of IO to investigate the impacts of CH_2OO + I (R4) and CH_2IO_2 + I (R7) on the subsequent production of IO using the mechanism given in Table 2. The rate coefficient used for R7 in the model shown in Table 2 is taken from the work of Gravestock *et al.*,[36] in which laser-induced fluorescence was employed to monitor the formation of IO and HCHO following photolysis of CH_2I_2/O_2 at 100 Torr, with kinetics determined by fitting to the HCHO observations. A mechanism producing IO directly from CH_2I + O_2 was found to be inconsistent with their observations, which led to the conclusion that the formation and subsequent reactions of CH_2IO_2 are the most likely to be responsible for IO production.

Production of IO in the system following the initial rapid production in this work potentially results from the chemistry of CH_2OO or CH_2IO_2, or a combination of the two. If produced through reactions of CH_2OO, IO can be produced either directly, via R4c, or indirectly, via R4b by way of production of CH_2IO_2 which then proceeds to generate IO through R7. Figure 5 indicates that R4b is the dominant channel of the CH_2OO + I reaction and that R4c does not occur since association reactions, such as R4b exhibit pressure dependence whereas bimolecular reactions, such as R4c do not. As the fit of the Lindemann equation through the experimental data (Figure 5) shows that at zero pressure the overall rate coefficient of R4 is zero or very small, this signifies that the contribution of R4c to the overall rate coefficient for R4 is not significant. Since R4a has already been excluded as a potential pathway for the reaction between CH_2OO and I at 298 K, this suggests that the only viable channel for this reaction is the production of the CH_2IO_2 peroxy radical. Figure 8 shows a typical comparison between observed and simulated IO profiles, constrained to the initial observed IO

concentration, in which R4 produces only CH_2IO_2 (i.e. R4b is the only reaction pathway considered). Simulations in which R4 produces 100 % CH_2IO_2 underpredict the observed IO at early times following photolysis where a growth is seen, and overpredict the observed IO at late time points following photolysis where the IO decay can be observed. This suggests that both the production and decay of IO in the system are underestimated in the model as listed in Table 2. This discrepancy between observed and simulated IO may be due to uncertainties in the chemistry of the CH_2IO_2 peroxy. To investigate whether this is the case, simulations were performed in which the rate coefficients for reactions involving CH_2IO_2 (R6 and R7) were increased and decreased, and the simulated IO profile was compared to the experimental data. Figure 8 shows that while increasing the rate coefficient for the CH_2IO_2 self-reaction brings the simulated IO at late times into agreement with the observed IO, it is still underestimated at early times. It can also be seen that increasing the rate coefficient for the CH_2IO_2 + I reaction increases the IO production such that the experimentally observed IO at early times is accounted for, however overestimates the IO at later times. On average, an increase in the rate coefficient for the CH_2IO_2 self-reaction of a factor of 3 was required in order to simulate an IO profile in agreement with the observed IO whereas the increase required for the rate coefficient of the CH_2IO_2 + I reaction is approximately a factor of 2. An example is given in Figure 8. These results suggest that kinetics of CH_2IO_2 chemistry in the model, in particular that of the CH_2IO_2 self-reaction, need to be significantly altered in order to account for the observed IO in the system. It should be noted that these adjustments to the rate coefficients of R6 and R7 show that a combination of changes to both rate coefficients may be required, and demonstrate the magnitude of these changes, in order to produce an IO simulation which can account for the IO observed in the system. However a quantitative analysis of CH_2IO_2 chemistry is outside the scope of this work. Results reported in this work for k_3 and k_4 include uncertainties arising from assumptions regarding rate coefficients and branching ratios used in the model given in Table 2.

The potential for reaction between CH_2OO and IO was also investigated in this work. However, results for k_3 and k_4 obtained by fitting to the observed CH_2OO profiles were not sensitive to the inclusion of a reaction between CH_2OO and IO in the model with a rate coefficient below 1×10^{-10} cm^3 s^{-1}, regardless of whether the model was constrained or unconstrained to the observed IO concentrations. Further details are provided in the Supplementary Information.

Conclusions

The UV absorption cross-sections of the Criegee Intermediate CH_2OO, and kinetics of the CH_2OO self-reaction and the reaction of CH_2OO with I have been investigated at a temperature of 298 K and pressures between 6 and 300 Torr using pulsed laser flash photolysis of $CH_2I_2/O_2/N_2$ gas mixtures coupled with time-resolved broadband UV absorption spectroscopy. Results indicate a broad UV absorption spectrum for CH_2OO, with a peak absorption cross-section of $(1.37 \pm 0.29) \times 10^{-17}$ cm^2 at $\lambda \sim 340$ nm and vibronic structure at wavelengths > 340 nm, in good agreement with results reported by Ting *et al.*[28] and Foreman *et al.*[29] Kinetics of the CH_2OO self-reaction have been shown to be independent of pressure over the range investigated, with a rate coefficient of $(8.0 \pm 1.1) \times 10^{-11}$ cm^3 s^{-1} over all pressures. The reaction CH_2OO + I is significant in the reaction system, with a pressure-dependent rate coefficient ranging from $(1.1\ ^{+2.2}_{-1.1}) \times 10^{-12}$ cm^3 s^{-1} at 6 Torr to $(5.5 \pm 2.1) \times 10^{-11}$ cm^3 s^{-1} at 300 Torr which can be parameterised by a Lindemann fit using $k_0 = (4.4 \pm 1.0) \times 10^{-29}$ cm^6 s^{-1} and $k_\infty = (6.7 \pm 0.6) \times 10^{-11}$ cm^3 s^{-1}. The production of IO in the system has also been investigated as a function of pressure. Results indicate that IO formation results from the chemistry of both CH_2OO and CH_2IO_2, with relative contributions from CH_2OO and CH_2IO_2 chemistry varying as a function of pressure owing to the pressure-dependent yields of CH_2OO and CH_2IO_2 from $CH_2I + O_2$ and the pressure dependence of the CH_2OO + I reaction.

Conflicts of interest

There are no conflicts of interest to declare.

Acknowledgements

The authors would like to thank the Natural Environment Research Council (NERC) for funding (grant references NE/L010798/1 and NE/P012876/1) and for the award of a studentship as part of the SPHERES DTP scheme.

Tables

Band centre / nm (This work)	FWHM / nm	Band centre / nm Ting *et al.*[28]	Band centre / nm Foreman *et al.*[29]
364.3	17.5	363.6	364.272
372.0	13.3	372.0	371.955
380.2	10.6	380.7	380.040
388.4	10.3	389.3	388.863
399.0	8.9	399.0	397.915
408.6	10.9	409.3	408.680
420.2	11.7	420.5	419.305
431.5	7.9	-	431.109

Table 1: Band centres and widths of the vibronic features observed in the CH_2OO spectrum. Ting *et al.*[28] report only seven of the features observed in this work and in the work of Foreman *et al.*[29] The weak feature centred at ~431 nm has been tentatively assigned as the band origin by Foreman *et al.*

Reaction Number	Reaction	Rate Coefficient, k / cm^3 s^{-1}	Reference
R2a	$CH_2I + O_2 \rightarrow CH_2OO + I$	$Y \times (1.5 \times 10^{-12})$	40, 50, 51
R2b	$CH_2I + O_2 \rightarrow CH_2IO_2$	$(1-Y) \times (1.5 \times 10^{-12})$	40, 50, 51
R3	$CH_2OO + CH_2OO \rightarrow 2\ HCHO + O_2$	k_3	Determined in fit
R4	$CH_2OO + I \rightarrow$ products	k_4	Determined in fit
R5	$CH_2OO \rightarrow$ loss	k_5 *	Determined in fit
R6	$CH_2IO_2 + CH_2IO_2 \rightarrow 2\ CH_2IO + O_2$	9.0×10^{-11}	36
R7	$CH_2IO_2 + I \rightarrow CH_2IO + IO$	3.5×10^{-11}	36
R8	$CH_2IO \rightarrow HCHO + I$	1.0×10^{5} *	36
R9	$IO + IO \rightarrow$ products	1.5×10^{-10}	32, 46

Table 2: Summary of the reactions and rate coefficients used in the model to fit to experimental observations of CH_2OO to determine the rate coefficients k_3, k_4 and k_5. Initial concentrations of CH_2OO were determined by fitting to the data, with initial concentrations of CH_2I, I and CH_2IO_2 determined from our previous measurements[40] of the yields of $CH_2I + O_2$, where Y indicates the yield of CH_2OO from $CH_2I + O_2$, and their relationship to the initial concentration of CH_2OO. *Units of s^{-1}.

Pressure / Torr	k_3 / 10^{-11} cm^3 s^{-1}	k_4 / 10^{-11} cm^3 s^{-1}
6	7.9 ± 1.1	$0.1\ ^{+0.2}_{-0.1}$
15	7.5 ± 1.0	2.2 ± 1.4
30	8.0 ± 1.2	2.4 ± 1.8
70	8.5 ± 1.0	4.3 ± 1.7
120	8.3 ± 1.1	4.3 ± 1.7
160	8.5 ± 1.1	5.1 ± 2.2
200	7.7 ± 1.1	6.2 ± 2.8
250	7.9 ± 1.3	5.4 ± 2.4
300	7.6 ± 1.0	5.5 ± 2.1

Table 3: Summary of results for the rate coefficients for the CH_2OO self-reaction (k_3) and CH_2OO + I (k_4) as a function of pressure. Values at each pressure are the mean values obtained over all experiments at that pressure. Uncertainties include the 1σ standard deviation of the mean values and the uncertainties determined from the fit sensitivities to reactions R6-R9 and the branching ratios for reaction R4.

Study	Temperature / K	Pressure / Torr	Photolysis λ / nm	Detection Technique	$[CH_2OO]_0$ / 10^{11} cm^{-3}	k_3 / 10^{-11} cm^3 s^{-1}	k_4
Su *et al*., 2014 [30]	343	10 – 100	355	FTIR	100 - 800	40 ± 20	$(4 \pm 2) \times 10^{-11}$ cm^3 s^{-1}
Buras *et al*., 2014 [31]	297	25 – 100	266	UVA	20 - 200	6.0 ± 2.1	$< 1 \times 10^{-11}$ cm^3 s^{-1}
Ting *et al*., 2014 [32]	295	7.6 – 779	248	UVA	200 - 2000	8.2 ± 1.4	$(6 – 10) \times 10^{-11}$ cm^3 s^{-1}
Chhantyal-Pun *et al*., 2015 [19]	293	7 – 30	355	CRDS	25 - 50	7.35 ± 0.63	$< 1 \times 10^{-11}$ cm^3 s^{-1}
This work	298	6 – 300	248	UVA	1 - 10	8.0 ± 1.1	$k_0 = (4.4 \pm 1.0) \times 10^{-29}$ cm^6 s^{-1}
							$k_\infty = (6.7 \pm 0.6) \times 10^{-11}$ cm^3 s^{-1}

Table 4: Summary of results for the rate coefficient for the CH_2OO self-reaction (k_3) and for the reaction between CH_2OO and I (k_4) obtained in this work and reported in the literature. FTIR = Fourier transform infrared; UVA = UV absorption; CRDS = cavity ringdown spectroscopy.

Figures

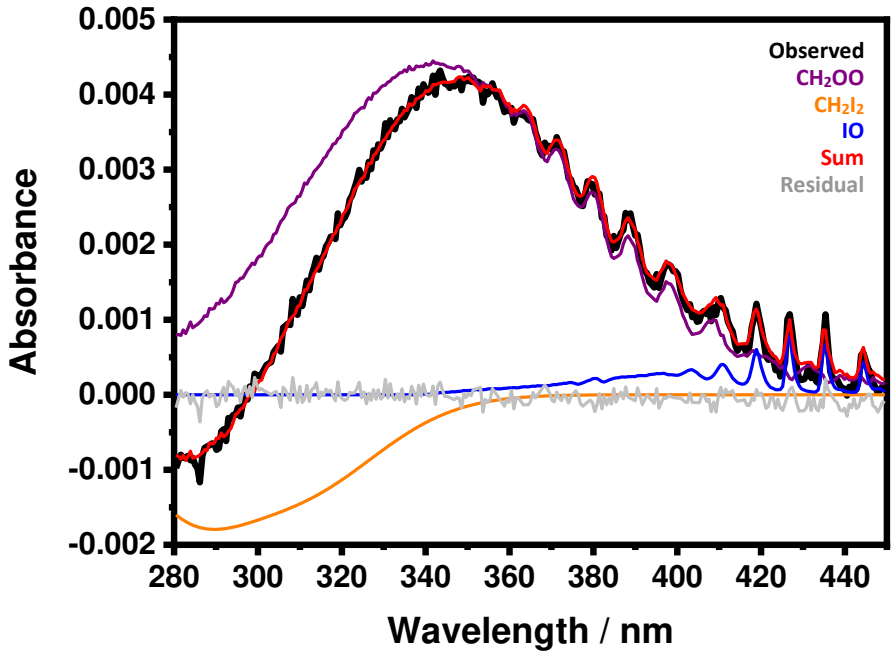

Figure 1: Total observed absorbance (A, black) at t = 1 ms following photolysis of $CH_2I_2/O_2/N_2$. Contributions from CH_2I_2, IO and CH_2OO determined by fitting reference spectra to the observed absorbance, and the fit residual, are also shown. For these data, p = 70 Torr, $[O_2] = 2.19 \times 10^{17}$ cm^{-3}, $[CH_2I_2] = 9.72 \times 10^{12}$ cm^{-3}, $\Delta[CH_2I_2]\ l = 6.06 \times 10^{14}$ cm^{-2}, $[CH_2OO]_0 = 7.27 \times 10^{11}$ cm^{-3}, $[CH_2OO] = 7.06 \times 10^{11}$ cm^{-3}, $[IO] = 1.96 \times 10^{11}$ cm^{-3}.

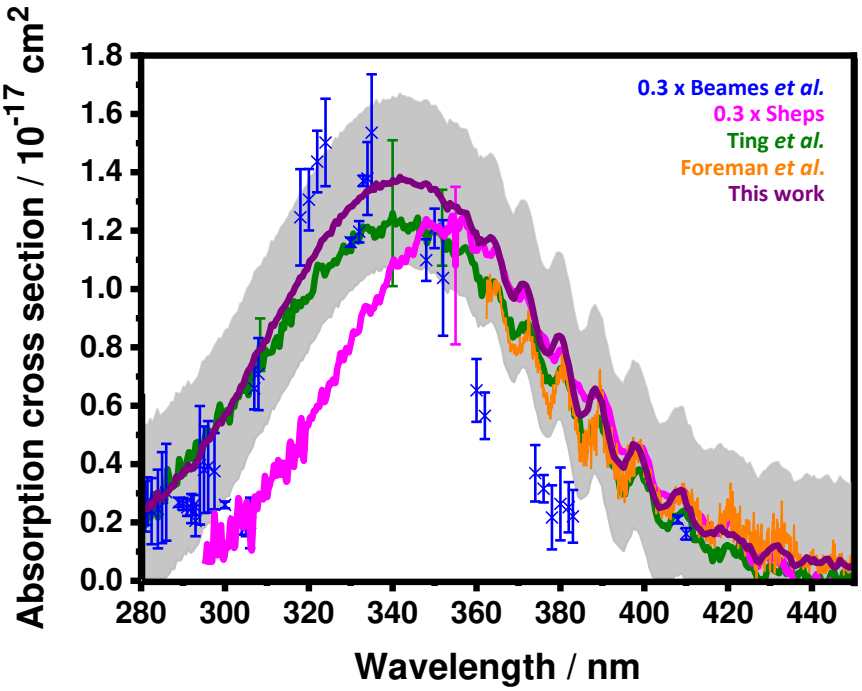

Figure 2: Absolute CH_2OO cross-sections determined in this work (purple line), with the 1σ standard deviation (grey shading). Results from previous work are also shown. Note that the results of Beames *et al.*[27] and Sheps[16] are scaled by a factor of 0.3.

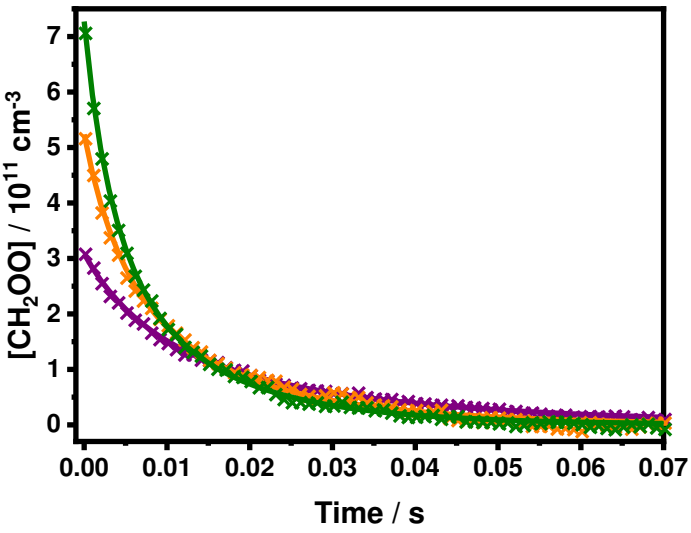

Figure 3: Temporal profile of the experimentally observed [CH_2OO] (green, orange and purple points) and the respective model fit (green, orange and purple line) using the mechanism given in Table 2. For all these data p = 70 Torr; for the data shown in green [O_2] = 2.19 × 10^{17} cm^{-3}, and [CH_2I_2] = 9.72 × 10^{12} cm^{-3}, and the fit to the data gave [CH_2OO]$_0$ = (7.27 ± 0.12) × 10^{11} cm^{-3}, k_3 = (9.5 ± 0.9) × 10^{-11} cm^3 s^{-1}, k_4 = (4.4 ± 0.4) × 10^{-11} cm^3 s^{-1} and k_5 = 0.030 ± 0.002 s^{-1}; for the data shown in orange [O_2] = 1.49 × 10^{17} cm^{-3}, and [CH_2I_2] = 1.91 × 10^{13} cm^{-3}, and the fit to the data gave [CH_2OO]$_0$ = (5.24 ± 0.11) × 10^{11} cm^{-3}, k_3 = (7.9 ± 0.4) × 10^{-11} cm^3 s^{-1}, k_4 = (5.0 ± 0.2) × 10^{-11} cm^3 s^{-1} and k_5 = 1.00 ± 0.21 s^{-1}; and for the data shown in purple [O_2] = 1.50 × 10^{17} cm^{-3}, and [CH_2I_2] = 7.25 × 10^{12} cm^{-3}, and the fit to the data gave [CH_2OO]$_0$ = (3.08 ± 0.13) × 10^{11} cm^{-3}, k_3 = (8.1 ± 1.3) × 10^{-11} cm^3 s^{-1}, k_4 = (5.0 ± 0.5) × 10^{-11} cm^3 s^{-1} and k_5 = 0.15 ± 0.27 s^{-1}.

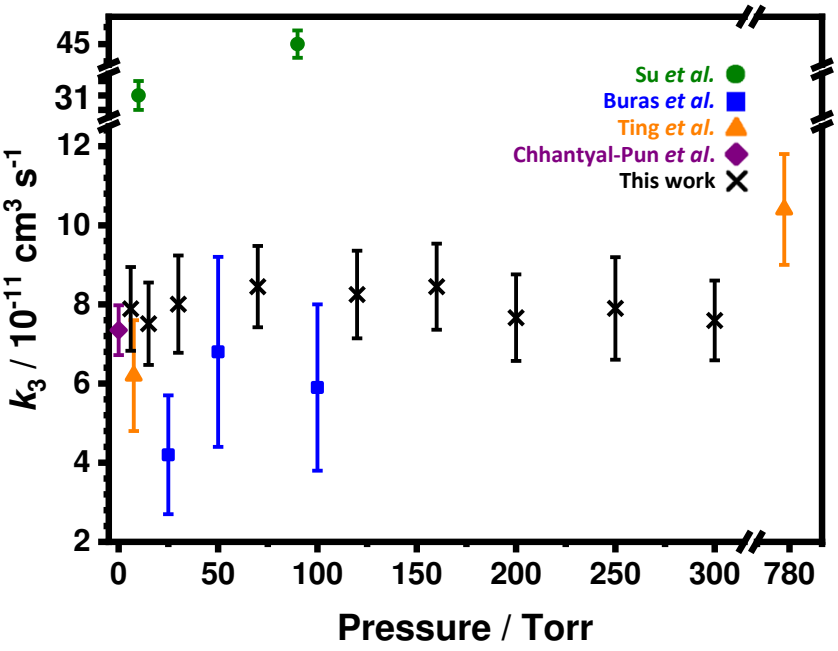

Figure 4: Rate coefficients for the CH_2OO self-reaction (k_3) as a function of pressure determined in this work (black points). Uncertainties include the 1σ standard deviation of the mean values and the uncertainties determined from the fit sensitivities to reactions R6-R9 and the branching ratios for reaction R4. Results reported in previous work are also shown.

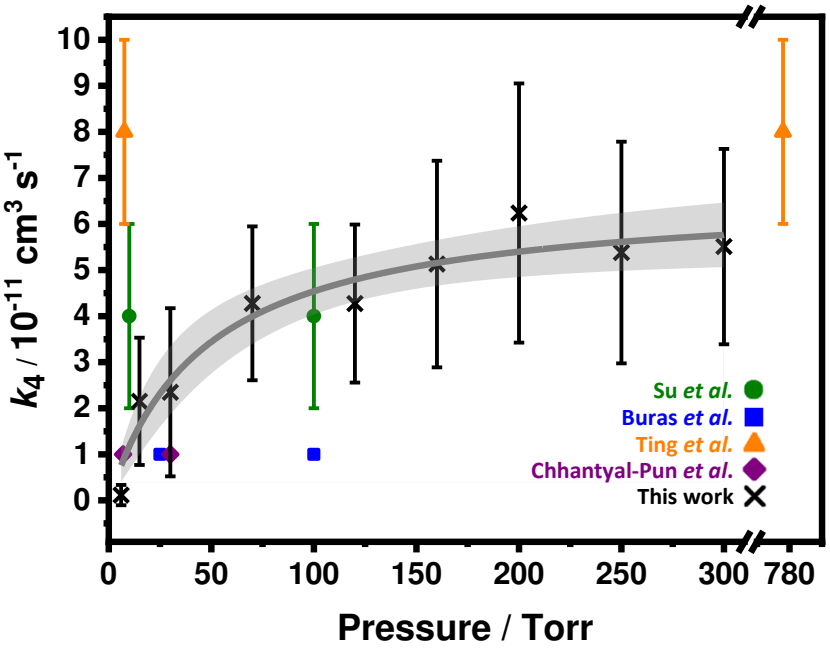

Figure 5: Rate coefficients for the reaction between CH_2OO and I (k_4) as a function of pressure determined in this work (black points). Uncertainties include the 1σ standard deviation of the mean values and the uncertainties determined from the fit sensitivities to reactions R6-R9 and the branching ratios for reaction R4. The fit to the Lindemann equation (Equation 3, shown by the grey line, with the 95 % confidence bands to the fit shown by the light grey shaded region) gives $k_{4,0} = (4.4 \pm 1.0) \times 10^{-29}$ cm^6 s^{-1} and $k_{4,\infty} = (6.7 \pm 0.6) \times 10^{-11}$ cm^3 s^{-1}.

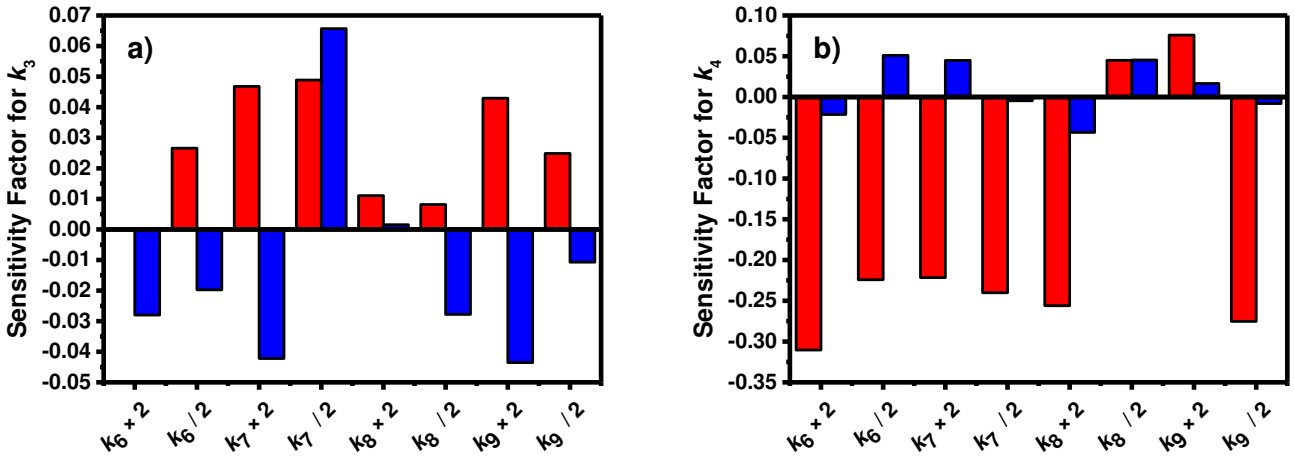

Figure 6: Sensitivity of a) k_3 and b) k_4 to the rate coefficients adopted in the model used to fit to experimental observations. Results are shown for analyses at 70 Torr (red) and 300 Torr (blue). The sensitivity factor is defined as the fractional difference in the fit result for a) k_3 and b) k_4 compared to the fit result determined using the rate coefficients as given in Table 2.

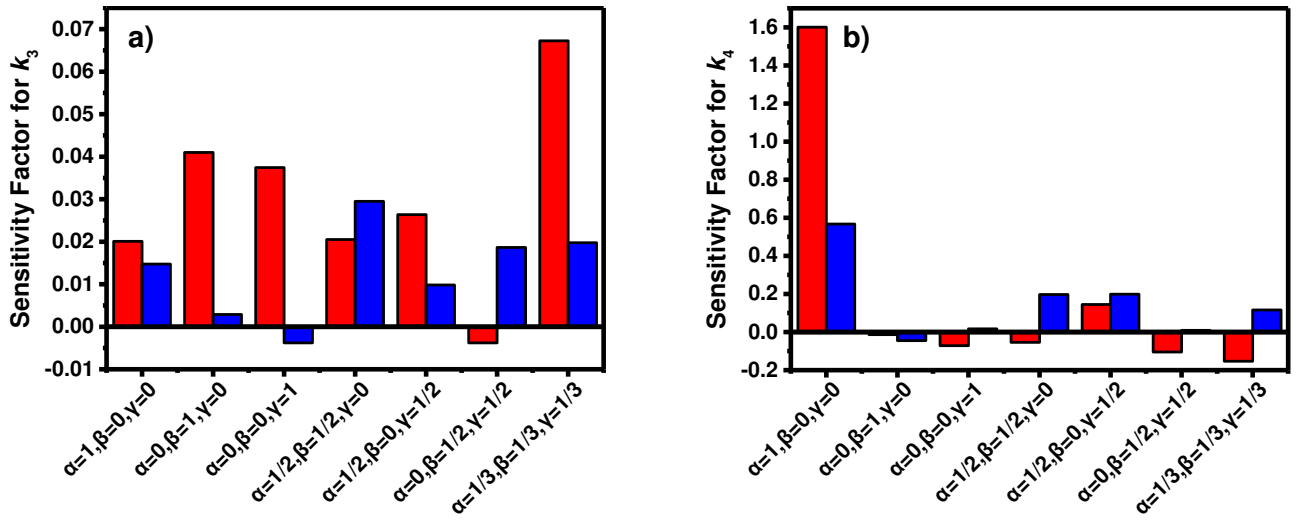

Figure 7: Sensitivity of a) k_3 and b) k_4 to the branching ratios adopted in the model for the reaction between CH_2OO and I (R4). Branching ratios are defined as α for channel R4a (producing $CH_2I + O_2$), β for channel R4b (producing CH_2IO_2), and γ for channel R4c (producing HCHO + IO). Results are shown for analyses at 70 Torr (red) and 300 Torr (blue). The sensitivity factor is defined as the fractional difference in the fit result for a) k_3 and b) k_4 compared to the result determined for fits in which no products for R4 are specified.

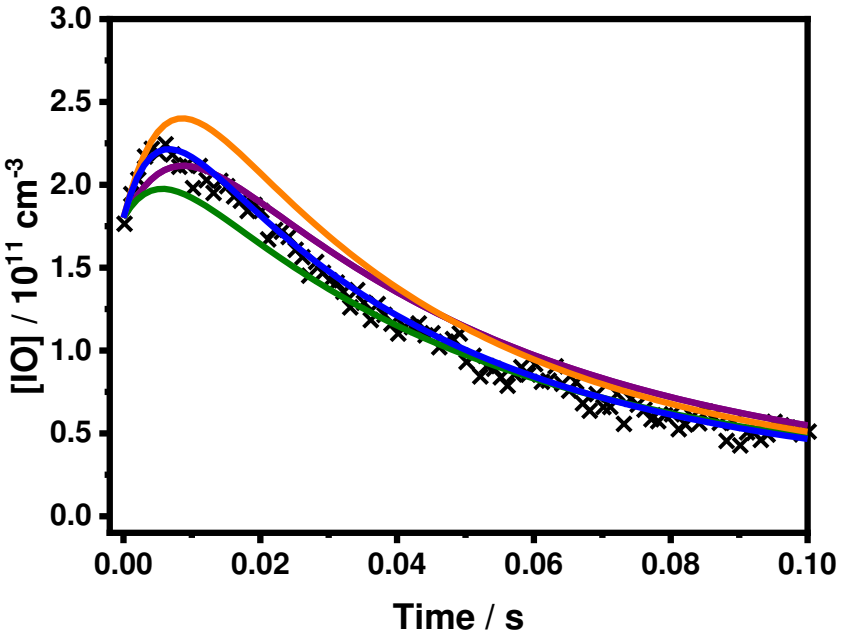

Figure 8: Experimentally observed IO concentrations (black points) and simulated IO profiles using the mechanism given in Table 2, except where specified otherwise, and constrained to the observed IO concentration at t = 1 ms. The reaction between CH_2OO and I (R4) was set to produce CH_2IO_2 with 100 % yield (purple). Adjustments made to the rate coefficients of the CH_2IO_2 self-reaction (R6) and the CH_2IO_2 + I reaction (R7) to simulate IO profiles which better represented the IO observed in the system than using rate coefficients as given in Table 2 were 3 × k_6 (green), 1.5 × k_7 (orange) and a combination of both 3 × k_6 and 1.5 × k_7 (blue). For these data, p = 70 Torr, $[O_2] = 1.49 \times 10^{17}$ cm^{-3}, $[CH_2I_2] = 1.57 \times 10^{13}$ cm^{-3}, and $[CH_2OO]_0 = 6.77 \times 10^{11}$ cm^{-3}. The comparison between observed and simulated IO profiles for data at p = 300 Torr is given in the Supplementary Information.

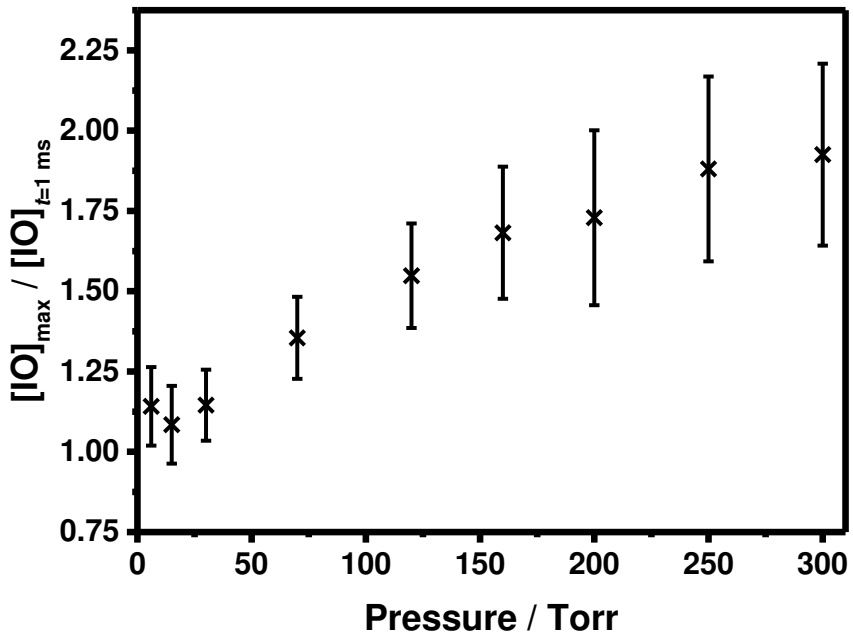

Figure 9: Ratio of the maximum observed IO concentration to the concentration of IO generated by the initial rapid production, representing the yield of IO produced in the system following the initial rapid growth, as a function of pressure. Uncertainties are the 1σ standard deviation of the mean values at each pressure.

References

1. Nguyen, T. B.; Tyndall, G. S.; Crounse, J. D.; Teng, A. P.; Bates, K. H.; Schwantes, R. H.; Coggon, M. M.; Zhang, L.; Feiner, P.; Milller, D. O.; Skog, K. M.; Rivera-Rios, J. C.; Dorris, M.; Olson, K. F.; Koss, A.; Wild, R. J.; Brown, S. S.; Goldstein, A. H.; Gouw, J. A. d.; Brune, W. H.; Keutsch, F. N.; Seinfeld, J. H.; Wennberg, P. O. *Physical Chemistry Chemical Physics* **2016,** 18, (15), 10241-10254.
2. Heard, D. E.; Carpenter, L. J.; Creasey, D. J.; Hopkins, J. R.; Lee, J. D.; Lewis, A. C.; Pilling, M. J.; Seakins, P. W.; Carslaw, N.; Emmerson, K. M. *Geophysical Research Letters* **2004,** 31, (18), L18112.
3. Harrison, R. M.; J.Yin; Tilling, R. M.; Cai, X.; Seakins, P. W.; Hopkins, J. R.; Lansley, D. L.; Lewis, A. C.; Hunter, M. C.; Heard, D. E.; Carpenter, L. J.; Creasey, D. J.; Lee, J. D.; Pilling, M. J.; Carslaw, N.; Emmerson, K. M.; Redington, A.; Derwent, R. G.; Ryall, D.; Mills, G.; Penkett, S. A. *Science of the Total Environment* **2006,** 360, (1-3), 5-25.
4. Stone, D.; Evans, M. J.; Walker, H.; Ingham, T.; Vaughan, S.; Ouyang, B.; Kennedy, O. J.; McLeod, M. W.; Jones, R. L.; Hopkins, J.; Punjabi, S.; Lidster, R.; Hamilton, J. F.; Lee, J. D.; Lewis, A. C.; Carpenter, L. J.; Forster, G.; Oram, D. E.; Reeves, C. E.; Bauguitte, S.; Morgan, W.; Coe, H.; Aruffo, E.; Dari-Salisburgo, C.; Giammaria, F.; Carlo, P. D.; Heard, D. E. *Atmospheric Chemistry and Physics* **2014,** 14, (3), 1299-1321.
5. Stone, D.; Whalley, L. K.; Heard, D. E. *Chemical Society Reviews* **2012,** 41, (19), 6348-6404.
6. Womack, C. C.; Martin-Drumel, M.-A.; Brown, G. G.; Field, R. W.; McCarthy, M. C. *Science Advances* **2015,** 1, (2), e1400105.
7. Malkin, T. L.; Goddard, A.; Heard, D. E.; Seakins, P. W. *Atmospheric Chemistry and Physics* **2010,** 10, (3), 1441-1459.
8. Donahue, N. M.; Drozd, G. T.; Epstein, S. A.; Prestoa, A. A.; Kroll, J. H. *Physical Chemistry Chemical Physics* **2011,** 13, (23), 10848-10857.
9. Novelli, A.; Vereecken, L.; Lelieveld, J.; Harder, H. *Physical Chemistry Chemical Physics* **2014,** 16, (37), 19941-19951.
10. Johnson, D.; Marston, G. *Chemical Society Reviews* **2008,** 37, (4), 699-716.
11. Welz, O.; Savee, J. D.; Osborn, D. L.; Vasu, S. S.; Percival, C. J.; Shallcross, D. E.; Taatjes, C. A. *Science* **2012,** 335, (6065), 204-207.
12. Chao, W.; Hsieh, J.-T.; Chang, C.-H.; Lin, J. J.-M. *Science* **2015,** 347, (6223), 751-754.
13. Lewis, T. R.; Blitz, M. A.; Heard, D. E.; Seakins, P. W. *Physical Chemistry Chemical Physics* **2015,** 17, (7), 4859-4863.
14. Smith, M. C.; Chang, C.-H.; Chao, W.; Lin, L.-C.; Takahashi, K.; Boering, K. A.; Lin, J. J.-M. *Journal of Physical Chemistry Letters* **2015,** 6, (14), 2708-2713.
15. Sheps, L.; Rotavera, B.; Eskola, A. J.; Osborn, D. L.; Taatjes, C. A.; Au, K.; Shallcross, D. E.; Khan, M. A. H.; Percival, C. J. *Physical Chemistry Chemical Physics* **2017,** 19, (33), 21970-21979.
16. Sheps, L. *The Journal of Physical Chemistry Letters* **2013,** 4, (24), 4201-4205.
17. Liu, Y.; Bayes, K. D.; Sander, S. P. *Journal of Physical Chemistry A* **2014,** 118, (4), 741-747.
18. Stone, D.; Blitz, M.; Daubney, L.; Howes, N. U. M.; Seakins, P. W. *Physical Chemistry Chemical Physics* **2014,** 16, (3), 1139-1149.
19. Chhantyal-Pun, R.; Davey, A.; Shallcross, D. E.; Percival, C. J.; Orr-Ewing, A. J. *Physical Chemistry Chemical Physics* **2015,** 17, (5), 3617-3626.
20. Taatjes, C. A.; Welz, O.; Eskola, A. J.; Savee, J. D.; Scheer, A. M.; Shallcross, D. E.; Rotavera, B.; Lee, E. P. F.; Dyke, J. M.; Mok, D. W. K.; Osborn, D. L.; Percival, C. J. *Science* **2013,** 340, (6129), 177-180.
21. Sheps, L.; Scully, A. M.; Au, K. *Physical Chemistry Chemical Physics* **2014,** 16, (48), 26701-26706.
22. Huang, H.-L.; Chao, W.; Lin, J. J.-M. *Proceedings of the National Academy of Sciences* **2015,** 112, (35), 10857-10862.
23. Smith, M. C.; Chao, W.; Takahashi, K.; Boering, K. A.; Lin, J. J.-M. *Journal of Physical Chemistry A* **2016,** 120, (27), 4789-4798.
24. Chhantyal-Pun, R.; Welz, O.; Savee, J. D.; Eskola, A. J.; Lee, E. P. F.; Blacker, L.; Hill, H. R.; Ashcroft, M.; Khan, M. A. H.; Lloyd-Jones, G. C.; Evans, L.; Rotavera, B.; Huang, H.; Osborn, D. L.; Mok, D. K. W.; Dyke, J. M.; Shallcross, D. E.; Percival, C. J.; Orr-Ewing, A. J.; Taatjes, C. A. *Journal of Physical Chemistry A* **2017,** 121, (1), 4-15.

25. Welz, O.; Eskola, A. J.; Sheps, L.; Rotavera, B.; Savee, J. D.; Scheer, A. M.; Osborn, D. L.; Lowe, D.; Booth, M.; Xiao, P.; Khan, M. A. H.; Percival, C. J.; Shallcross, D. E.; Taatjes, C. A. *Angewandte Chemie International Edition* **2014,** 53, (18), 4547-4550.
26. Chhantyal-Pun, R.; McGillen, M. R.; Beames, J. M.; Khan, M. A. H.; Percival, C. J.; Shallcross, D. E.; Orr-Ewing, A. J. *Angewandte Chemie International Edition* **2017,** 56, (31), 9044-9047.
27. Beames, J. M.; Liu, F.; Lu, L.; Lester, M. I. *Journal of the American Chemical Society* **2012,** 134, (49), 20045-20048.
28. Ting, W.-L.; Chen, Y.-H.; Chao, W.; Smith, M. C.; Lin, J. J.-M. *Physical Chemistry Chemical Physics* **2014,** 16, (22), 10438-10443
29. Foreman, E. S.; Kapnas, K. M.; Jou, Y.; Kalinowski, J.; Feng, D.; Gerber, R. B.; Murray, C. *Physical Chemistry Chemical Physics* **2015,** 17, (48), 32539-32546.
30. Su, Y.-T.; Lin, H.-Y.; Putikam, R.; Matsui, H.; Lin, M. C.; Lee, Y.-P. *Nature Chemistry* **2014,** 6, (6), 477–483.
31. Buras, Z. J.; Elsamra, R. M. I.; Green, W. H. *The Journal of Physical Chemistry Letters* **2014,** 5, (13), 2224-2228.
32. Ting, W.-L.; Chang, C.-H.; Lee, Y.-F.; Matsui, H.; Lee, Y.-P.; Lin, J. J.-M. *The Journal of Chemical Physics* **2014,** 141, (10), 104308.
33. Chhantyal-Pun, R.; Khan, M. A. H.; Martin, R.; Zachhuber, N.; Buras, Z. J.; Percival, C. J.; Shallcross, D. E.; Orr-Ewing, A. J. *ACS Earth and Space Chemistry* **2019,** 3, (10), 2363-2371.
34. Lee, E. P. F.; Mok, D. K. W.; Shallcross, D. E.; Percival, C. J.; Osborn, D. L.; Taatjes, C. A.; Dyke, J. M. *Chemistry - A European Journal* **2012,** 18, (39), 12411-12423.
35. Dawes, R.; Jiang, B.; Guo, H. *Journal of the American Chemical Society* **2015,** 137, (1), 50-53.
36. Gravestock, T. J.; Blitz, M. A.; Bloss, W. J.; Heard, D. E. *ChemPhysChem* **2010,** 11, (18), 3928-3941.
37. Beames, J. M.; Liu, F.; Lu, L.; Lester, M. I. *The Journal of Chemical Physics* **2013,** 138, (24), 244307.
38. Huang, H.; Eskola, A. J.; Taatjes, C. A. *The Journal of Physical Chemistry Letters* **2012,** 3, (22), 3399-3403.
39. Huang, H.; Rotavera, B.; Eskola, A. J.; Taatjes, C. A. *The Journal of Physical Chemistry Letters* **2013,** 4, (22), 3824.
40. Stone, D.; Blitz, M.; Daubney, L.; Ingham, T.; Seakins, P. *Physical Chemistry Chemical Physics* **2013,** 15, (44), 19119-19124
41. Vereecken, L.; Harder, H.; Novelli, A. *Physical Chemistry Chemical Physics* **2014,** 16, (9), 4039-4049.
42. Lewis, T.; Heard, D. E.; Blitz, M. A. *Review of Scientific Instruments* **2018,** 89, (2), 024101.
43. Keller-Rudek, H.; Moortgat, G. K.; Sander, R.; Sörensen, R. *Earth System Science Data* **2013,** 5, 365–373.
44. Sršeň, Š.; Hollas, D.; Slavíček, P. *Physical Chemistry Chemical Physics* **2018,** 20, (9), 6421-6430.
45. *FACSIMILE Kinetic Modelling Software*, MCPA Software Ltd: 2014.
46. Atkinson, R.; Baulch, D. L.; Cox, R. A.; Crowley, J. N.; Hampson, R. F.; Hynes, R. G.; Jenkin, M. E.; Rossi, M. J.; Troe, J. *Atmospheric Chemistry and Physics* **2007,** 7, (4), 981–1191.
47. Vereecken, L.; Hardera, H.; Novellia, A. *Physical Chemistry Chemical Physics* **2012,** 14, (42), 14682-14695.
48. Anglada, J. M.; Olivella, S.; Solé, A. *Physical Chemistry Chemical Physics* **2013,** 15, (43), 18921-18933.
49. Miliordos, E.; Xantheas, S. S. *Angewandte Chemie International Edition* **2016,** 55, (3), 1015 –1019.
50. Masaki, A.; Tsunashima, S.; Washida, N. *The Journal of Physical Chemistry* **1995,** 99, (35), 13126-13131.
51. Eskola, A. J.; Wojcik-Pastuszka, D.; Ratajczak, E.; Timonen, R. S. *Physical Chemistry Chemical Physics* **2006,** 8, (12), 1416-1424.
52. Enami, S.; Ueda, J.; Goto, M.; Nakano, Y.; Aloisio, S.; Hashimoto, S.; Kawasaki, M. *The Journal of Physical Chemistry A* **2004,** 108, (30), 6347-6350.
53. Enami, S.; Sakamoto, Y.; Yamanaka, T.; Hashimoto, S.; Kawasaki, M.; Tonokura, K.; Tachikawa, H. *Bulletin of the Chemical Society of Japan* **2008,** 81, (10), 1250-1257.
54. Dillon, T. J.; Tucceri, M. E.; Sander, R.; Crowley, J. N. *Physical Chemistry Chemical Physics* **2008,** 10, (11), 1540-1554.
55. Foreman, E. S.; Murray, C. *The Journal of Physical Chemistry A* **2015,** 119, (34), 8981-8990.

56. Stone, D.; Au, K.; Sime, S.; Medeiros, D. J.; Blitz, M.; Seakins, P. W.; Decker, Z.; Sheps, L. *Physical Chemistry Chemical Physics* **2018,** 20, (38), 24940-24954.